THE JOURNAL OF CHEMICAL PHYSICS **141**, 124503 (2014)

Calculating two-dimensional THz-Raman-THz and Raman-THz-THz signals for various molecular liquids: The samplers

Hironobu Ito,[1,a)] Taisuke Hasegawa,[1,2,b)] and Yoshitaka Tanimura[1,c)]
[1] *Department of Chemistry, Graduate School of Science, Kyoto University, Sakyoku, Kyoto 606-8502, Japan*
[2] *Department of Physics, University of Hamburg, Centre for Free Electron Laser Science, DESY, Notkestrasse 85, D-22607 Hamburg, Germany*

(Received 23 June 2014; accepted 5 September 2014; published online 23 September 2014)

Recently, two-dimensional (2D) THz-Raman spectroscopy has been used to investigate the intermolecular modes of liquid water. We examine such 2D spectroscopy signals by means of full molecular dynamics (MD) simulations. In this way, we carry out a detailed analysis of intermolecular interactions that play an essential role in many important chemical processes. We calculate 2D Raman-THz-THz (RTT), THz-Raman-THz (TRT), and 2D Raman signals for liquid water, methanol, formamide, acetonitrile, formaldehyde, and dimethyl sulfoxide using an equilibrium-non-equilibrium hybrid MD simulation algorithm originally developed for 2D Raman spectroscopy. These signals are briefly analyzed in terms of anharmonicity and nonlinear polarizability of vibrational modes on the basis of the 2D Raman signals calculated from a Brownian oscillator model with a nonlinear system-bath interaction. We find that the anharmonic contribution is dominant in the RTT case, while the nonlinear polarizability contribution is dominant in the TRT case. For water and methanol, we observed vibrational echo peaks of librational motion in the 2D TRT signals. The predicted signal profiles and intensities that we obtained provide valuable information that can be applied to 2D spectroscopy experiments, allowing them to be carried out more efficiently. © *2014 Author(s). All article content, except where otherwise noted, is licensed under a Creative Commons Attribution 3.0 Unported License.* [http://dx.doi.org/10.1063/1.4895908]

I. INTRODUCTION

Understanding dynamics in complex environments of molecular liquids and biological systems has been a central topic of investigation in chemistry and biology, because many important chemical processes occur exclusively in such media. In the early 1990s, two-dimensional (2D) Raman spectroscopy was proposed for the analysis of intermolecular vibrational motion of liquid molecules. This led to the development of multi-dimensional spectroscopy methods, whose spectra are obtained by recording the signals as functions of the time durations between trains of pulses.[1,2] Multi-dimensional spectroscopy signals are expressed in terms of nonlinear response functions that are defined with respect to the molecular dipole moment or the polarizability.[3] Notable examples of 2D spectroscopy for vibrational motion are fifth-order 2D Raman spectroscopy[4–52] and third-order 3D infrared (IR) spectroscopy.[53–66]

In 1D vibrational spectroscopy, for which signals are defined in terms of linear response functions of the optical observables, the main contribution to a signal arises from harmonic vibrational motion, while the signal contribution from anharmonicity is weak in comparison to the harmonic one. Contrastingly, in multi-dimensional vibrational spectroscopy, the anharmonicity of potentials as well as anharmonic mode couplings contribute significantly to a signal, because the anharmonic motion is the leading-order contribution in the nonlinear response functions, while the harmonic contributions vanish. Thus, linear vibrational spectroscopy can be regarded as the analysis of harmonic molecular motion, while multi-dimensional vibrational spectroscopy can be regarded as the analysis of anharmonic molecular motion.[27,66]

Among the vibrational types of motion, intermolecular vibrations play an essential role in many important chemical reaction processes, because they allow to relax the energy of intramolecular vibrations supplied by chemical reaction processes very rapidly through the nonlinear coupling between the intramolecular motions and intermolecular librational motions.[67–72] For the investigation of this kind of motion, 2D Raman spectroscopy is more advantageous than 2D IR spectroscopy, because Raman process can be used to excite and detect intermolecular motion directly. 2D Raman spectroscopy was originally proposed to detect homogeneous and inhomogeneous broadenings of liquid dynamics.[4,5] Intensive studies investigating the application of 2D Raman spectroscopy to the observation of these and other types of phenomena have been carried out through theoretical modeling,[4–27] molecular dynamics (MD) simulations,[28–41] and experiments.[44–52] However, in such studies, it was found that it is difficult to measure fifth-order Raman signals, due to cascading effects that arise from a sequence of third-order Raman signals with the same power dependence and direction as the desired 2D Raman signal.[44] This difficulty was overcome through various methods developed independently

---

[a)] Electronic mail: h.ito@kuchem.kyoto-u.ac.jp
[b)] Electronic mail: hasegawa@kuchem.kyoto-u.ac.jp
[c)] Electronic mail: tanimura@kuchem.kyoto-u.ac.jp

by the Fleming group[47] and the Miller group,[49] however 2D Raman spectroscopy remains technically challenging, and for this reason, reliable 2D signals have been obtained only for CS_2,[47–50] benzene,[51] and formamide liquids,[52] which exhibit strong Raman polarizability. Note that THz pulses can be used instead of Raman pulses to probe intermolecular motion,[73,74] but 2D THz spectroscopy has been applied only to solid-state materials,[75–77] because the energy of THz pulses is still too small with current technology.

Recently, a new spectroscopic approach, 2D THz-Raman spectroscopy has been developed.[78–80] In this approach, cascading effects are suppressed, because it involves only one Raman process, in contrast to 2D Raman spectroscopy, in which three Raman processes are involved. Although there remain some technical difficulties in the application of 2D THz-Raman spectroscopy due to the electromagnetic wave nature of the THz field and limitations on the pulse strength, it is expected that 2D THz-Raman spectroscopy will have a wider applicability than 2D Raman spectroscopy. At this time, reliable 2D THz-Raman signals have been reported for liquid water.[80]

As in the case of 2D Raman spectroscopy, however, the analysis of 2D THz-Raman signals is somewhat complicated, because the target of 2D THz-Raman spectroscopy consists of low frequency collective modes that arise from the varieties of translational, vibrational, and librational motion of molecules. Fortunately, theories and simulation techniques developed for 2D Raman spectroscopy can also be applied to analyze the signals of 2D THz-Raman spectroscopy, because these signals are defined in terms of three-body correlation functions of optical observables. In the 2D Raman case, theoretical analyses have been carried out to elucidate the inhomogeneous broadening of molecules,[4,5] the anharmonicity of the vibrational potentials,[6–14] the vibrational mode coupling between the intramolecular and intermolecular modes,[15–18] and the dephasing process.[19–27] MD simulation techniques applied to the calculation of 2D Raman signals have been developed to investigate various molecular liquids.[28–41]

In the case of 2D IR spectroscopy, the MD simulation can be utilized to parameterize a theoretical model, because the primary intermolecular modes, which are the objects of study in 2D IR spectroscopy, can be separated from the other bath modes, as in the case of the OH stretching mode in liquid water.[60] Contrastingly in the 2D Raman and 2D THz-Raman cases, it is not easy to find primary modes, because the objects of study in these cases are the collective modes. Thus, we have to evaluate 2D signals directly from the MD simulations (the full MD simulation approach).[30–41] Because quantum mechanical effects are minor for low-frequency intermolecular modes at room temperature, unlike the case of intramolecular motion,[65] and because 2D THz-Raman spectroscopy employs the three-body correlation function with two time variables, instead of the four-body correlation function with three time variables employed in 3D IR spectroscopy,[81] the full MD simulation approach is practical.

To carry out full MD simulations, the equilibrium stability matrix approach,[30–38] the non-equilibrium finite field approach,[39,40] and the equilibrium-non-equilibrium hybrid MD approach[41] have been developed. In the equilibrium approach, the stability matrix in the nonlinear response function is evaluated by considering the equilibrium molecular trajectories. Because the convergence of the stability matrix for different MD trajectories is very slow,[42,43] a large amount of storage space and powerful CPUs are required for simulations. With the non-equilibrium approach, there is no stability matrix, but in this case, a great deal of computational power is needed to subtract off lower-order field contributions to the response. To address these problems, the hybrid method has been developed. This method retains the desirable features of the equilibrium MD methods, while eliminating the need to calculate the stability matrix, because the observable of interest is generated through use of a finite field perturbation. In this way, the computational requirements are greatly reduced.[41]

The full MD approach yields predictions of signal profiles and signal intensities. Given the technical difficulties involved in experiments, this information is valuable in application to 2D experiments, allowing for greater efficiency in their performance. In addition, while 2D profiles are sensitive to variations in the potential, which is created in a phenomenological manner,[52] the full MD approach allows us to confirm the validity of the MD simulation, because we can compare the MD results directly to experimental results. Then, on the basis of simulational and experimental results, we can apply theoretical models to analyze the signals. In this way, experimental measurements, full MD simulations, and theoretical model analyses can be used in a complementary manner to investigate the fundamental nature of intermolecular interactions.

In this paper, we explore the sensitivity of 2D THz-Raman spectroscopy by means of a full MD simulation utilizing an equilibrium-non-equilibrium hybrid MD simulation algorithm. With this approach, we calculated the 2D signals for liquid water, methanol, formamide, acetonitrile, formaldehyde, and dimethyl sulfoxide (DMSO). Here, these calculated signals are briefly analyzed on the basis of Brownian oscillator models with a nonlinear system-bath interaction developed for 2D Raman spectroscopy. We evaluated the relative signal intensities for these molecular liquids with the goal of providing information that will allow experiments to be carried out more efficiently.

In Sec. II, we present the equilibrium-non-equilibrium hybrid algorithm used to calculate the 2D THz-Raman-THz and Raman-THz-THz response functions. In Sec. III, we explain the theoretical framework analyzing 2D THz-Raman signals. In Sec. IV, we describe the computational details for the simulations of the molecular liquids studied here, the samplers. Then, we present and discuss the results of the 2D THz-Raman simulations in Sec. V. The 2D Raman signals for the same molecular liquids are presented and discussed in Appendix A. Section VI is devoted to concluding remarks.

II. EQUILIBRIUM-NON-EQUILIBRIUM HYBRID MD ALGORITHM

We consider a molecular liquid system described by a Hamiltonian $H_0(\mathbf{p},\mathbf{q})$, where $\mathbf{p}$ and $\mathbf{q}$ represent the momenta and position coordinates of the molecules, respectively. The

2D THz-Raman-THz (TRT) and Raman-THz-THz (RTT) signals are expressed in terms of the third-order nonlinear response functions defined by the molecular dipole moment and polarizability.[78,79] In the quantum mechanical case, these signals are given by

$$R^{(3)}_{TRT}(t_2, t_1) = \left(\frac{i}{\hbar}\right)^2 \langle[[\boldsymbol{\mu}(t_1 + t_2), \boldsymbol{\Pi}(t_1)], \boldsymbol{\mu}(0)]\rangle, \tag{1}$$

$$R^{(3)}_{RTT}(t_2, t_1) = \left(\frac{i}{\hbar}\right)^2 \langle[[\boldsymbol{\mu}(t_1 + t_2), \boldsymbol{\mu}(t_1)], \boldsymbol{\Pi}(0)]\rangle, \tag{2}$$

where $\boldsymbol{\mu}(\mathbf{t})$ and $\boldsymbol{\Pi}(\mathbf{t})$ are the dipole moment and the polarizability of the molecules expressed as functions of the molecular positions $\mathbf{q}$ at time t, respectively. In Appendix A, we also present the expressions for the 2D Raman signals.

The classical mechanical expression for the response functions can be obtained by replacing the commutator with the Poisson bracket as $i[\cdots,\cdots]/\hbar \rightarrow \{\cdots,\cdots\}_{PB}$, where

$$\{\mathbf{A}, \mathbf{B}\}_{PB} \equiv \frac{\partial \mathbf{A}}{\partial \mathbf{q}}\frac{\partial \mathbf{B}}{\partial \mathbf{p}} - \frac{\partial \mathbf{A}}{\partial \mathbf{p}}\frac{\partial \mathbf{B}}{\partial \mathbf{q}}, \tag{3}$$

for any functions $\mathbf{A}$ and $\mathbf{B}$. To simulate the three-body response function, three full molecular dynamics simulation approaches, namely, the equilibrium stability matrix approach,[30–38] the non-equilibrium finite field approach,[39,40] and the equilibrium-non-equilibrium hybrid MD approach,[41] have been developed. Here, we adopt the hybrid approach, which requires less computational capacity than the other two approaches by retaining the desirable features of both the equilibrium MD and non-equilibrium MD in the calculation of the 2D signal. Using the time-transversal symmetry of the response function, we have $\langle\{\{\mathbf{A}'(t_1 + t_2), \mathbf{A}''(t_1)\}_{PB}, \mathbf{B}(0)\}_{PB}\rangle = \langle\{\{\mathbf{A}'(t_2), \mathbf{A}''(0)\}_{PB}, \mathbf{B}(-t_1)\}_{PB}\rangle$. In the hybrid approach, the outer Poison bracket is replaced by the time derivative of the observable at time $-t_1$ as $\langle\{\mathbf{A}(t), \mathbf{B}(-t_1)\}_{PB}\rangle = -\beta\langle\mathbf{A}(t)\dot{\mathbf{B}}(-t_1)\rangle$, where β is the inverse temperature divided by the Boltzmann constant, k_B, and $\dot{\mathbf{B}}(-t_1) = d\mathbf{B}(t)/dt|_{t=-t_1}$. In equilibrium-non-equilibrium hybrid MD simulation algorithm,[41] we evaluate the time derivative of $\mathbf{B}$ with equilibrium MD simulations, while we evaluate the others with non-equilibrium MD (NEMD) simulations. We calculate $\Delta\mu_{\Pi(0)}(t_2) = \{\boldsymbol{\mu}(t_2), \boldsymbol{\Pi}(0)\}_{PB}$ and $\Delta\mu_{\mu(0)}(t_2) = \{\boldsymbol{\mu}(t_2), \boldsymbol{\mu}(0)\}_{PB}$ for the TRT and RTT signals, respectively. In the NEMD simulation, they are evaluated from the MD trajectories with an impulsive external potential, $V(t)$, applied at $t = 0$. Thus, the full Hamiltonian becomes

$$H(\mathbf{p}, \mathbf{q}) = H_0(\mathbf{p}, \mathbf{q}) + V(t). \tag{4}$$

Here, we regard $V(t)$ to be the interaction of the system with the laser applied in the spectroscopy experiment. For the TRT and RTT calculations, $V(t)$ represents the Raman and IR interactions, respectively, given by

$$V_R(t) = -\frac{1}{2}\mathbf{E}_1(t)\Pi\mathbf{E}_2(t), \tag{5}$$

$$V_T(t) = -\mathbf{E}_1(t)\mu, \tag{6}$$

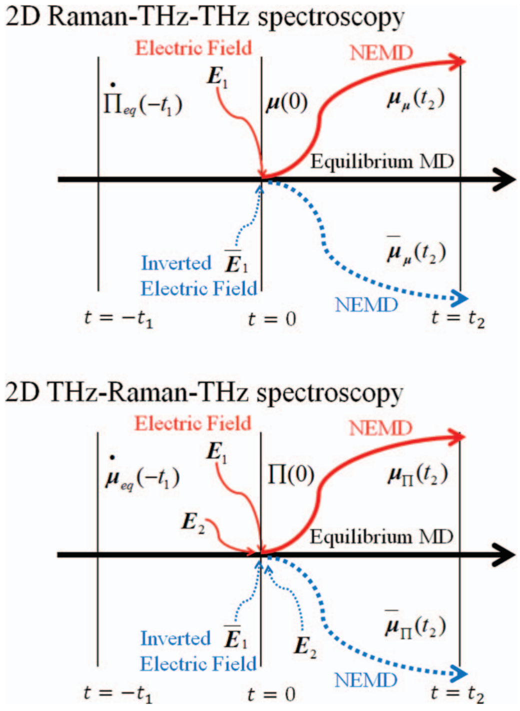

FIG. 1. Schematic representations of the hybrid MD simulations for 2D THz-Raman-THz (TRT) spectroscopy and Raman-THz-THz (RTT) spectroscopy. The black line denotes the equilibrium trajectories, and the red and blue lines denote the non-equilibrium trajectories perturbed by external electric fields and inverted external electric fields, respectively.

where $\mathbf{E}_1(t) = \mathbf{E}_1\delta(t)$ and $\mathbf{E}_2(t) = \mathbf{E}_2\delta(t)$. The expectation values of the dipole moment at time t_2 with a perturbation applied at time $t = 0$, $\mu_{\Pi(0)}(t_2)$ and $\mu_{\mu(0)}(t_2)$, are evaluated from the trajectories with the perturbations given in Eqs. (5) and (6), respectively. To obtain $\Delta\mu_{\Pi(0)}(t_2)$ and $\Delta\mu_{\mu(0)}(t_2)$, we must subtract the equilibrium expectation values, calculated from the MD trajectories without the perturbation. This can be done efficiently by subtracting the expectation values $\bar{\mu}_{\Pi(0)}(t_2)$ and $\bar{\mu}_{\mu(0)}(t_2)$ that are calculated from the trajectories with the inverse force fields, i.e., $\Delta\mu_{\Pi(0)}(t_2) = \mu_{\Pi(0)}(t_2) - \bar{\mu}_{\Pi(0)}(t_2)$ and $\Delta\mu_{\mu(0)}(t_2) = \mu_{\mu(0)}(t_2) - \bar{\mu}_{\mu(0)}(t_2)$, as illustrated in Fig. 1.[40] Then, the response functions in the THz-Raman-THz and Raman-THz-THz cases can be expressed as

$$R^{(3)}_{TRT}(t_2, t_1) = \frac{2\beta}{E_1 E_2}\langle(\mu_{\Pi(0)}(t_2) - \overline{\mu}_{\Pi(0)}(t_2))\dot{\mu}_{eq}(-t_1)\rangle, \tag{7}$$

and

$$R^{(3)}_{RTT}(t_2, t_1) = \frac{\beta}{E_1}\langle(\mu_{\mu(0)}(t_2) - \overline{\mu}_{\mu(0)}(t_2))\dot{\Pi}_{eq}(-t_1)\rangle, \tag{8}$$

where E_j is the external electric field of the jth pulse. The expression for the 2D Raman signal is given in Appendix A.

III. CHARACTERISTIC FEATURES OF TWO-DIMENSIONAL THZ-RAMAN SIGNALS

A. Anharmonic interactions

In order to analyze the results of the simulations of 2D TRT spectroscopy and RTT spectroscopy systems, it is helpful to employ a Brownian oscillator model developed for 2D Raman spectroscopy. In the study of vibrational spectroscopy, response functions are expressed in terms of the dipole moment $\mu(\mathbf{q}')$ and/or polarizability $\Pi(\mathbf{q}'')$, which depend on the molecular coordinates of the IR active modes, $\mathbf{q}'$, as $\mu(\mathbf{q}') = \mu_0 + \mu_1\mathbf{q}' + \mu_2\mathbf{q}' \cdot \mathbf{q}' + \cdots$ and the Raman active modes, $\mathbf{q}''$, as $\Pi(\mathbf{q}'') = \Pi_0 + \Pi_1\mathbf{q}'' + \Pi_2\mathbf{q}'' \cdot \mathbf{q}'' + \cdots$, respectively. Note that the intermolecular modes are usually both IR and Raman active, i.e., $\mathbf{q} \propto \mathbf{q}' \sim \mathbf{q}''$, because there is no symmetry to distinguish the IR and Raman active modes for low-frequency collective modes.

In the 2D Raman case, the signal is expressed as $\langle[[\hat{\mathbf{\Pi}}(t_{12}), \hat{\mathbf{\Pi}}(t_1)], \hat{\mathbf{\Pi}}(0)]\rangle$ for $t_{12} = t_1 + t_2$, as shown in Appendix A, while 2D TRT and RTT response functions are expressed as $\langle[[\hat{\boldsymbol{\mu}}(t_{12}), \hat{\mathbf{\Pi}}(t_1)], \hat{\boldsymbol{\mu}}(0)]\rangle$ and $\langle[[\hat{\boldsymbol{\mu}}(t_{12}), \hat{\boldsymbol{\mu}}(t_1)], \hat{\mathbf{\Pi}}(0)]\rangle$, respectively. If the interaction potentials are harmonic, their lowest-order terms, e.g., $\mu_1^2\mathbf{\Pi}_1\,\langle[[\mathbf{q}'(t_{12}), \mathbf{q}'(t_1)], \mathbf{q}''(0)]\rangle$, do not contribute to the signal, because the ensemble averages of the correlation functions involved in the response function, e.g., $tr\{\mathbf{q}'(t_{12})\mathbf{q}'(t_1)\mathbf{q}''(0)\exp[-\beta H_0(\mathbf{p}, \mathbf{q})]\}$, become Gaussian integrals of odd order in $\mathbf{q}'$ or $\mathbf{q}''$. However, if the interaction potentials are anharmonic[6–14] or if there are anharmonic mode-mode couplings,[15–18] the lowest-order contribution survives, because the ensemble averages are no longer Gaussian integrals. The signal from this term appears along the t_2 axis with a time delay of $\Delta t_2 \approx 1/2\omega$ from the t_1 axis, where ω is the characteristic frequency of the vibrational mode, and hence we can distinguish this contribution from the other contributions.[6,14] The experimentally obtained signal for CS_2 indicates the existence of anharmonic contributions.[47–49]

B. Vibrational dephasing and energy relaxation

When the nonlinear elements of the dipole moment μ_2 and/or polarizability Π_2 are large, we can observe a signal even if the anharmonic interactions are weak, because the thermal averages become Gaussian integrals of even order in $\mathbf{q}'$ and $\mathbf{q}''$, due to the nonlinear dipole and polarizability elements, e.g., $\langle[[\mathbf{q}'(t_{12}), \mathbf{q}'(t_1)], \mathbf{q}''^2(0)]\rangle$ and $\langle[[\mathbf{q}'(t_{12}), \mathbf{q}''^2(t_1)], \mathbf{q}'(0)]\rangle$.[4,5]

Among the contributions from the nonlinear polarizability, we can often distinguish the term $\langle[[\mathbf{q}'(t_{12}), \mathbf{q}''^2(t_1)], \mathbf{q}'(0)]\rangle$ from the others, because this term exhibits an echo peak along the diagonal direction, i.e., $t_1 = t_2$, which is useful for estimating the dephasing time scale.[4,5,19–22] The mechanism responsible for the echo peak from this term has been described using the energy diagrammatic representation.[19–22] This description is presented in Appendix B. In the pure homogeneous case of 2D Raman spectroscopy, however, the contribution from the nonlinear polarizability exhibits non-decaying peaks along the t_2 axis and in the $t_1 = t_2$ direction.[4,24] When vibrational energy relaxation takes place, these peaks decay in time,[23–27] and we can explore the time scale and mechanism of vibrational relaxation from these signal profiles.

Note that in 2D IR spectroscopy, for the intramolecular modes of a solute molecule, the effects of energy relaxation are usually ignored, while dephasing is not. This is because the excitation energies of the solute modes are much higher than the energies of the solvation bath modes, and hence the energy transfer from intra-molecular modes to the bath modes is inefficient.[63–66] In the 2D Raman and 2D THz-Raman cases, however, both relaxation and dephasing are important, because the vibrational energies of intermolecular modes are very close to the thermal energy. In order to include the effects of energy relaxation, we employ an oscillator model with a nonlinear and non-Markovian system-bath interaction instead of a phenomenological stochastic model.[27] The 2D Raman signals calculated with this model describe the difference between the 2D profiles for the inhomogeneous case and the homogeneous case in a unified manner as a function of the noise correlation time induced by the bath modes.

C. Two-dimensional THz-Raman-THz and Raman-THz-THz signals

While 2D TRT, 2D RTT, and 2D Raman signals are all defined in terms of the three-body response functions, the information obtained from 2D TRT and 2D RTT spectroscopy measurements can be different from that obtained from 2D Raman spectroscopy measurements, because the nonlinearity of the dipole elements is weaker than that of the polarizability. This is because the dipole moment is a linear function of the distance between the charges, while the nonlinear dipole-induced dipole interactions are weak. Contrastingly, because the polarizability originates from the electronic states of molecules, which depend on the complex configurations of the atoms and molecules, the nonlinear elements of the polarizability are not small. Hence, we have $\mu_1^2\Pi_2 \gg \mu_1\mu_2\Pi_1$. Thus, while the terms $\langle[[\mathbf{q}''(t_{12}), \mathbf{q}''(t_1)], \mathbf{q}''^2(0)]\rangle$, $\langle[[\mathbf{q}''(t_{12}), \mathbf{q}''^2(t_1)], \mathbf{q}''(0)]\rangle$, and $\langle[[\mathbf{q}''^2(t_{12}), \mathbf{q}''(t_1)], \mathbf{q}''(0)]\rangle$ contribute equally in the 2D Raman case, illustrated Eq. (A3), the first one is larger than the others in the case of 2D RTT spectroscopy, whereas the second is larger than the others in the case of 2D TRT spectroscopy. These signals are expressed as

$$R^{(3)}_{TRT}(t_2, t_1) = \mu_1^2\Pi_1\,\langle[[\mathbf{q}'(t_{12}), \mathbf{q}''(t_1)], \mathbf{q}'(0)]\rangle + \mu_1^2\Pi_2\,\langle[[\mathbf{q}'(t_{12}), \mathbf{q}''^2(t_1)], \mathbf{q}'(0)]\rangle\,, \quad (9)$$

$$R^{(3)}_{RTT}(t_2, t_1) = \mu_1^2\Pi_1\,\langle[[\mathbf{q}'(t_{12}), \mathbf{q}'(t_1)], \mathbf{q}''(0)]\rangle + \mu_1^2\Pi_2\,\langle[[\mathbf{q}'(t_{12}), \mathbf{q}'(t_1)], \mathbf{q}''^2(0)]\rangle\,. \quad (10)$$

Some representative Feynman diagrams involved in Eqs. (9) and (10) are presented in Appendix B. Because the second term in Eq. (9) is responsible for the echo peak, and because there are no other contributions to order $\mu_1^2\Pi_2$ in the case of TRT spectroscopy, we should be able to observe an echo signal in the TRT signal that is clearer than that in the 2D Raman signal.

IV. COMPUTATIONAL DETAILS

We calculated the 2D TRT and RTT signals for water, methanol, formamide, acetonitrile, formaldehyde, and DMSO

TABLE I. Computational details employed for each molecular liquid in the 2D THz-Raman-THz (TRT), Raman-THz-THz (RTT), and 2D Raman (2DR) simulations.

Molecule	Potential	Polarizability	ρ (g/cm^3)	T (K)	E[a] (V/Å)		N_{samp}[b] ($\times 10^6$)	
					V_R	V_T	TRT, 2DR	RTT
Water	TIP4P/2005[84]	Huiszoon[91]	0.997	300	5.0	1.0	1.36	1.36
Methanol	B3[85]	Atomic[83]	0.786	300	5.0	1.0	1.36	1.36
Formamide	Modified T[86,87]	Atomic[83]	1.120	300	5.0	2.5	1.20	1.20
Acetonitrile	6-site model[88]	Atomic[83]	0.777	300	5.0	5.0	0.96	1.92
Formaldehyde	4-site model[89]	Atomic[83]	0.815	260	2.0	2.5	1.36	1.36
DMSO	4-site model[90]	(see Appendix C)	1.100	300	4.0	5.0	3.20	4.80

[a] The intensities of the external electrical fields applied in the NEMD simulations to evaluate the 2D TRT, 2DR, and 2D RTT response functions.

[b] The numbers of initial configurations used to evaluate the 2D TRT, 2DR, and 2D RTT response functions.

liquids using MD simulations. The simulations included 108 molecules, with periodic boundary conditions in a cubic box. Using the same conditions, we also calculated the 2D Raman signals presented in Appendix A. Full-order dipole-induced dipole models[82,83] were employed to evaluate the total dipole moment and polarizability at the center of mass in all simulations. The interaction potentials and polarizability were cut off smoothly at the half length of the system boxes using a switching function. The long-range Coulomb interactions and charge-induced dipole interactions were calculated with the EWALD sum. The intramolecular geometries were kept rigid for all simulations, with the constraint provided by the RATTLE algorithm. The equations of motion were integrated using the velocity-Verlet algorithm with time steps of 2.5 fs. The volume and energy were fixed after the completion of the isothermal simulations carried out for equilibration. The simulation models and conditions accompanying selected values of the average density, ρ, and temperature, T, for each molecular liquid are listed in Table I.

V. RESULTS AND DISCUSSION

A. Formaldehyde and dimethyl sulfoxide

We first consider polar nonprotic solvents exhibiting simple 2D profiles. Figures 2(a) and 2(b) display the *zzzz* tensor elements of the third-order (I) TRT and (II) RTT response functions for formaldehyde and DMSO liquids, respectively. In each figure, a nearly symmetric signal peak along the $-t_1 = t_2$ axis in the TRT region is observed, while an elongated negative peak along the t_2 axis is observed in the RTT region. The characteristic features of the positive peak in the TRT region and the negative peak in the RTT region are similar to those of a peak that arises from the nonlinear polarizability and a peak that arises from the anharmonicity in a pure dephasing case,[23–27] respectively, as illustrated by the 2D signals for an anharmonic oscillator with nonlinear system-bath interaction presented in Appendix D. This indicates that, while the dominant contribution to the TRT signal is from the nonlinear polarizability, $\mu_1^2\Pi_2\,\langle[[\mathbf{q}'(t_{12}), \mathbf{q}''^2(t_1)], \mathbf{q}'(0)]\rangle$, that to the RTT signal is from the anharmonicity of molecular interactions, $\mu_1^2\Pi_1\,\langle[[\mathbf{q}'(t_{12}), \mathbf{q}'(t_1)], \mathbf{q}''(0)]\rangle$. Although the effect is minor, we also observe an anharmonic contribution in the TRT case, appearing as the negative peak along the t_2 axis.

In the case of formaldehyde, the peak in the TRT region extends very close to the t_1 and t_2 axes, while in the case of DMSO is elongated along the $-t_1 = t_2$ line. Results of numerical calculations carried out for a system-bath model presented in Fig. 4 of Ref. 24 indicate that the damping in the formaldehyde case is much stronger than that in the DMSO case. Because of the strong damping, the negative anharmonic peak for formaldehyde near the t_2 axis is more strongly suppressed in the t_1 directions than that for DMSO.

B. Formamide and acetonitrile

Figures 3(a) and 3(b) display the *zzzz* tensor elements of the (I) 2D TRT and (II) 2D RTT signals for formamide and acetonitrile, respectively. The profiles in these cases are similar to those in the formaldehyde and DMSO cases, but the peak in the case of formamide is slightly elongated in the $-t_1$ and t_2 directions. This indicates that the damping in the case of formamide is weaker than that in the previous cases.

While the TRT and RTT signals are similar in the formamide, acetonitrile, formaldehyde, and DMSO cases, the 2D

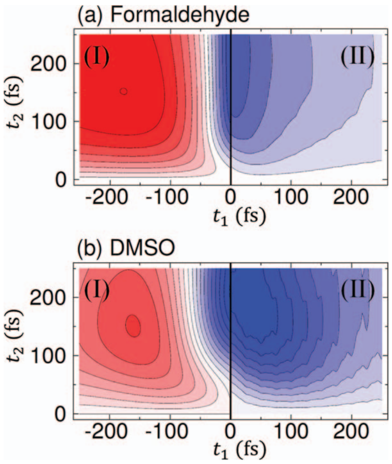

FIG. 2. The *zzzz* tensor elements of (I) the 2D THz-Raman-THz (TRT) signal and (II) the Raman-THz-THz signal (RTT) for (a) formaldehyde and (b) DMSO liquids, respectively. Positive and negative signals are represented by red and blue colors, respectively, and the time axis t_1 has been inverted in the TRT cases. The TRT and RTT signals have been normalized with respect to the maximum peak intensity of the TRT signal.

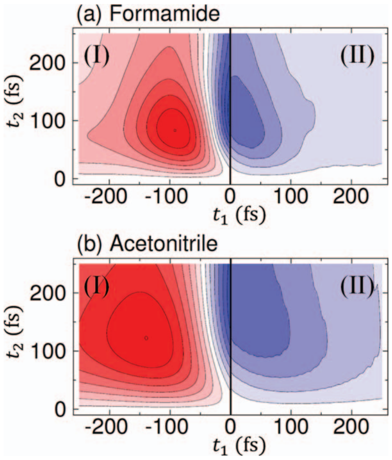

FIG. 3. The *zzzz* tensor elements of (I) the 2D THz-Raman-THz (TRT) signal and (II) the Raman-THz-THz signal (RTT) for (a) formamide and (b) acetonitrile liquids, respectively. Positive and negative signals are represented by red and blue colors, respectively, and the time axis t_1 has been inverted in the TRT cases. The TRT and RTT signals have been normalized with respect to the maximum peak intensity of the TRT signal.

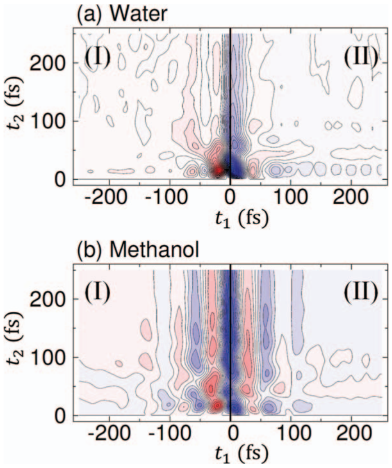

FIG. 4. The *zzzz* tensor elements of (I) the 2D THz-Raman-THz (TRT) signal and (II) the Raman-THz-THz signal (RTT) for (a) water and (b) methanol liquids, respectively. Positive and negative signals are represented by red and blue colors, respectively, and the time axis t_1 has been inverted in the TRT cases. The TRT and RTT signals have been normalized with respect to the maximum peak intensity of the TRT signal.

Raman signals for these liquids are quite different, as shown by Fig. 5 in Appendix A. This is because the 2D Raman signals arise from a variety of terms, which can be positive or negative, depending on the signs of the nonlinear polarizability and anharmonicity. The differences seen in Fig. 5 indicate that there is information that can be obtained only from 2D Raman spectroscopy. Thus, we conclude that 2D THz-Raman and 2D Raman spectroscopy measurements are complementary, although the applicability of 2D Raman spectroscopy is still limited.

C. Water and methanol

The simulation results for the *zzzz* tensor elements of (I) the TRT response function and (II) the RTT response function for water and methanol liquids are presented in Figs. 4(a) and 4(b), respectively. The results for water are similar to those obtained in Refs. 78 and 79. Note that the signs of the signals in the previous results are opposite of those for the present results, because the i^2 factor in the third-order response function was ignored in the results.

We find that 2D profiles for water and methanol differ dramatically from those for the other four liquids. This is because water and methanol form cluster structures via hydrogen bonds that change rapidly in time through fast translational and librational motion.

In both water and methanol, the TRT signals are similar to the 2D Raman signal calculated using a non-Markovian Brownian model with a nonlinear system-bath interaction that was introduced to describe a vibrational dephasing, as presented in Fig. 14(iii-b) of Ref. 27, while the RTT signals are similar to that calculated using a non-Markovian anharmonic Brownian model with a nonlinear system-bath interaction, as presented in Fig. 14(iii-a) of Ref. 27. This implies that the dominant contributions to the TRT signal is that from $\mu_1^2\Pi_2\,\langle[[\mathbf{q}'(t_{12}), \mathbf{q}''^2(t_1)], \mathbf{q}'(0)]\rangle$, while the dominant contribution to the RTT signal is that from $\mu_1^2\Pi_1\,\langle[[\mathbf{q}'(t_{12}), \mathbf{q}'(t_1)], \mathbf{q}''(0)]\rangle$.

In both figures, elongated peaks parallel to the t_2 axis appear in both the TRT and RTT regions. Their cause should be attributed to the anharmonicity of vibrational motion that may be described by an anharmonic non-Markovian Brownian model with a nonlinear system-bath interaction, as observed in the anharmonic case in Ref. 27. Because the decay of these peaks is faster in the case of water than in the case of methanol, we conclude that the energy relaxation of librational motion of water is faster than that of methanol indicating the coupling strength of hydrogen bonds in water is stronger than that in methanol. In the TRT case, we observe a peak along the line $-t_1 = t_2$. This peak is attributable to the vibrational echo peaks that arise from the librational motion.[35]

D. Signal intensities

One significant advantage of calculating 2D signals using a full MD approach is its capability to estimate the signal intensities for different liquids. Such information can be used when conducting experiments and reduce the effort needed to detect a signal. In Table II, we list the relative intensities of the 2D TRT, RTT, and 2D Raman signals for the molecular liquids investigated here, as evaluated from the maximum peak strength. We normalized the intensities of the TRT and RTT signals with respect to that for liquid water in the TRT region. As references, we also list the intensities of the *zz* element for the 1D THz response, $R_T^{(1)}(t_1) = \beta\,\langle\mu(t_1)\dot{\mu}(0)\rangle$, and the *zzzz* element for the 1D Raman response, $R_R^{(3)}(t_1) = \beta\,\langle\Pi(t_1)\dot{\Pi}(0)\rangle$, for all samples. It is seen that the intensities of the 2D TRT signals are stronger than those of the RTT signals, on average. This is because the nonlinear polarizability contribution in the TRT case, $\mu_1^2\Pi_2\,\langle[[\mathbf{q}'(t_{12}), \mathbf{q}''^2(t_1)], \mathbf{q}'(0)]\rangle$, is stronger than that in the RTT case, $\mu_1^2\Pi_2\,\langle[[\mathbf{q}'(t_{12}), \mathbf{q}'(t_1)], \mathbf{q}''^2(0)]\rangle$, due to the

TABLE II. Relative intensities of the 1D THz, 1D Raman, 2D THz-Raman-THz (TRT), 2D Raman-THz-THz (RTT) and 2D Raman (2DR) signals for the molecular liquids studied here. Each signal intensity is divided by the system volume. The 1D THz, 1D Raman, and 2D Raman signal intensities are normalized with respect to the intensity of the water signal, while the 2D TRT and RTT signals are normalized with respect to the 2D TRT intensity of the water signal. The ratio of the RTT and TRT signal intensities, $I_{RTT/TRT} = |R^{(3)}_{RTT}|/|R^{(3)}_{TRT}|$, and the estimated signal intensity, $R_{\mathrm{est}} = \sqrt{R^{(1)}_{T} \cdot R^{(1)}_{T} \cdot R^{(3)}_{R}}$, are also displayed.

Molecule	$\lvert R^{(1)}_{T}\rvert$	$\lvert R^{(3)}_{R}\rvert$	$\lvert R^{(3)}_{TRT}\rvert$	$\lvert R^{(3)}_{RTT}\rvert$	$I_{RTT/TRT}$	$\lvert R_{\mathrm{est}}\rvert$	$\lvert R^{(5)}_{2DR}\rvert$
Water	1	1	1	1.01	1.01	1	1
Methanol	0.213	1.23	0.476	0.386	0.811	0.355	3.76
Formamide	0.266	13.3	0.712	0.416	0.584	1.453	25.0
Acetonitrile	0.175	4.40	0.385	0.230	0.599	0.630	11.1
Formaldehyde	0.419	14.9	1.38	0.924	0.669	2.144	64.7
DMSO	0.130	2.07	0.0628	0.0618	0.983	0.371	2.49

oscillatory factors depicted in Fig. 6(iv), in contrast to the rephasing echo case depicted in Fig. 6(ii). It is shown that the 2D RTT and TRT signals for water are strong among the molecular liquids investigated here, while the 2D Raman signal is weakest for water, because of its weak anisotropic polarizability. In the 2D Raman case, the trend of the signal intensities among the liquids is determined by the magnitude of the polarizability.[41] Using the calculated 1D THz and 1D Raman intensities, we estimated the signal intensity of the 2D THz Raman response as $R_{\mathrm{est}} = \sqrt{R^{(1)}_{T} \cdot R^{(1)}_{T} \cdot R^{(3)}_{R}}$. The results obtained in this manner are qualitatively consistent with the general trend observed among the intensities, but they do not account quantitatively for individual values of the intensities listed in Table II. This is because the anharmonicity, nonlinear polarizability, and the different selection rules for the THz and Raman signals also play important roles in determining the signal intensities in 2D THz-Raman spectroscopy.

Except in the DMSO case, the 2D THz-Raman signals obtained for the other liquids are not weak compared to that for water. This suggests that it is possible to measure these signals experimentally. In addition, the 2D Raman signal for formaldehyde should be detectable, because the signal obtained in our simulations is stronger than the formamide signal, which has been observed experimentally.[52]

VI. CONCLUSIONS

We calculated the 2D TRT, RTT, and 2D Raman signals for water, methanol, formamide, acetonitrile, formaldehyde, and DMSO utilizing an equilibrium-non-equilibrium hybrid MD simulation algorithm. While the 2D signal profiles of formamide, acetonitrile, formaldehyde, and DMSO are similar and featureless, that of water and methanol exhibit rich profiles, reflecting the fast librational and translational motions with dephasing and relaxation. We demonstrated that the dominant contribution to the 2D RTT signal arises from the anharmonicity of molecular interactions, while that to the 2D TRT signal arises from the nonlinear polarizability, which is sensitive to the dephasing process characterized by an echo peak.

In this paper, we analyze the calculated signals using the previously calculated 2D Raman signals based on the Brownian model with nonlinear system-bath interaction. To investigate the role of the nonlinear polarizability, anharmonicity, energy relaxation, and dephasing of vibrational modes for the 2D TRT and RTT signals, we need to calculate the TRT and RTT signals separately as shown in Appendix D. In the case of water and methanol, non-Markovian and non-perturbative system-bath interactions play an essential role as indicated by the model calculations of 2D Raman signals. The intensive model calculations based on non-Markovian and non-perturbative Fokker-Planck equations have to be carried out for varieties of physical conditions to identify the key features of dynamics. We will leave it for future studies.

In this work, we used a rigid molecular model for all liquids, and we did not consider intra-molecular vibrational motion. Although the potential models and polarization function employed here are widely used, we feel that they are not sufficiently accurate to reliably calculate 2D signals, because the 2D profiles of nonlinear response functions are extremely sensitive to the accuracy of the potential and polarization functions, as illustrated by the 2D Raman profiles of formamide.[52] In addition, the impulsive laser excitation used here is not realistic in the case of THz spectroscopy, because the frequency of the pulse used in experiments is so small that the pulse profile becomes a fragment of a sinusoidal function.

In order to make a direct comparison between the results of our simulations and experimentally obtained results,[80] we must address the above points by modifying the potential and polarization functions in accordance with experimental systems. Nevertheless, we believe that the present results elucidate the key features of 2D TRT and 2D RTT spectroscopy methods with regard to probing the fundamental nature of intermolecular interactions.

ACKNOWLEDGMENTS

The authors would like to thank Professor Peter Hamm and Professor Shinji Saito for helpful discussions and Mr. Tatsushi Ikeda for providing the figure in Appendix D. The authors are grateful to Professor Dwayne J. Miller and his group members at DESY for their hospitality. Financial support provided by a Grant-in-Aid for Scientific Research (A26248005) from the Japan Society for the Promotion of Science is acknowledged.

APPENDIX A: FIFTH-ORDER TWO-DIMENSIONAL RAMAN SIGNALS

The fifth-order response function in 2D Raman spectroscopy is expressed in terms of the molecular polarizability as

$$R^{(5)}_{2DR}(t_2, t_1) = \left(\frac{i}{\hbar}\right)^2 \langle[[\mathbf{\Pi}(t_1 + t_2), \mathbf{\Pi}(t_1)], \mathbf{\Pi}(0)]\rangle. \quad \text{(A1)}$$

For the polarizability, $\Pi(\mathbf{q}'') = \Pi_0 + \Pi_1\mathbf{q}'' + \Pi_2\mathbf{q}'' \cdot \mathbf{q}'' + \cdots$, where $\mathbf{q}''$ is the molecular coordinate of the Raman active mode, this is expressed as

$$\begin{aligned} R^{(5)}_{2DR}(t_2, t_1) = {} & \Pi_1^3 \langle[[\mathbf{q}''(t_{12}), \mathbf{q}''(t_1)], \mathbf{q}''(0)]\rangle \\ & + \Pi_1^2\Pi_2 \langle[[\mathbf{q}''(t_{12}), \mathbf{q}''(t_1)], \mathbf{q}''^2(0)]\rangle \\ & + \Pi_1^2\Pi_2 \langle[[\mathbf{q}''(t_{12}), \mathbf{q}''^2(t_1)], \mathbf{q}''(0)]\rangle \\ & + \Pi_1^2\Pi_2 \langle[[\mathbf{q}''^2(t_{12}), \mathbf{q}''(t_1)], \mathbf{q}''(0)]\rangle\,, \quad \text{(A2)} \end{aligned}$$

where $t_{12} = t_1 + t_2$. Compared with the response functions for the 2D TRT and RTT cases given in Eqs. (9) and (10), the 2D Raman response function involves a variety of terms that arise from the nonlinear polarizability.

In the equilibrium-non-equilibrium hybrid MD approach, the fifth-order response function is evaluated from the classical MD as[41]

$$R^{(5)}_{2DR}(t_2, t_1) = \frac{2\beta}{E_1E_2}\langle(\mathbf{\Pi}_{\mathbf{\Pi}}(\mathbf{0})(t_2) - \overline{\mathbf{\Pi}}_{\mathbf{\Pi}(0)}(t_2))\dot{\mathbf{\Pi}}_{eq}(-t_1)\rangle, \quad \text{(A3)}$$

with the laser-interaction given in Eq. (5).

Under the same conditions as in the RTT and TRT cases presented in Table I, we also calculated the *zzzzzz* tensor elements of the fifth-order response functions for the molecular liquids investigated here. The results are presented in Fig. 5. Note that the oscillatory behavior of the DMSO and formamide signals in the t_1 direction is an artifact of the slow convergence signal evaluated from the time derivative of the polarizabilities.

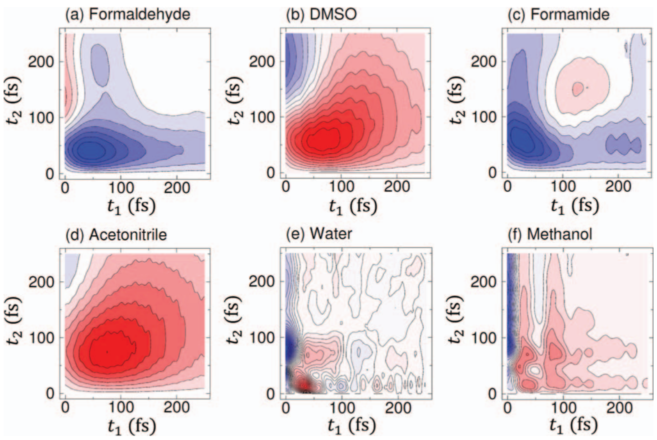

FIG. 5. The *zzzzzz* tensor elements for the fifth-order response functions of (a) formaldehyde, (b) DMSO, (c) formamide, (d) acetonitrile, (e) water, and (f) methanol in the case of 2D Raman spectroscopy. Positive and negative signals are represented by red and blue colors, respectively, and the signal intensities are normalized with respect to the absolute value of the peak signal intensities.

The 2D Raman signals for water, displayed in Fig. 5(e), and acetonitrile, displayed in Fig. 5(d), are very similar to the previous results presented in Fig. 2(a) of Ref. 35 and Fig. 6(a) of Ref. 41, respectively. The calculated formamide signal appearing in Fig. 5(c) is closer to the results given in Ref. 41 than those given in Ref. 52. This is because, although we employed the same potential, here we used the full-order polarization function,[82,83] while the results given in Ref. 52 were obtained using the first-order polarization function.

Although formaldehyde, DMSO, formamide, and acetnitorile exhibit similar 2D profiles in the cases of 2D TRT and RTT spectroscopy, they do not in the 2D Raman case. This is because many contributions of various magnitudes and signs from the anharmonicity and nonlinear polarizability are superimposed in the 2D Raman case. Nevertheless, we found that the TRT signals for acetnitorile, DMSO, water, and methanol are similar to the 2D Raman signals plotted in Figs. 5(b), 5(d), 5(e), and 5(f), respectively. This indicates that the contribution of the nonlinear polarizability is stronger than that of the anharmonicity in these liquids.

We observed echo signals in the water and methanol cases. A detailed mode analysis of the 2D Raman signal for liquid water was carried out by means of an equilibrium MD simulation.[29,35] It was shown that the echo signal on the $t_1 = t_2$ line arises from $\Pi_1^2\Pi_2 \langle[\mathbf{q}''(t_1 + t_2), [\mathbf{q}''^2(t_1), \mathbf{q}''(0)]]\rangle$. In the 2D Raman case, however, because the other contributions from the anharmonicity and nonlinear polarizability are superimposed on the echo signal, identification of the echo peak is not as easy as in the 2D TRT case.

In Table II, we list the relative intensities of the fifth-order response functions for the liquids investigated here. It is seen that the signal intensity of acetonitrile is approximately 10 times stronger than that for water. This result differs from that given in Ref. 41, because the present results were obtained using the full-order dipole-induced dipole model, while those given in Ref. 41 were obtained using the first-order one. The signal intensities for methanol and DMSO are weak, while that for formaldehyde is stronger than that measured experimentally for formamide.[52] This suggests that we should be able to detect the 2D Raman signal for formaldehyde experimentally.

APPENDIX B: OPTICAL LIOUVILLE PATHS FOR TWO-DIMENSIONAL THZ-RAMAN-THZ AND RAMAN-THZ-THZ SPECTROSCOPY

In this appendix, we present some representative double-sided Feynman diagrams involved in 2D TRT and RTT spectroscopy. Note that a quantum diagrammatic approach is helpful to gain insight into the underlying processes and to elucidate the 2D signal profiles even in the case of a classical MD simulation, because classical and quantum mechanical dynamics yield little discrepancy in the case of vibrational motion if the anharmonicity is very weak. While a THz pulse can create only one quantum excitation or de-excitation, denoted by $\mu_1\mathbf{q}'$, a Raman pulse can create a double excitation through the large nonlinear polarizability, denoted by $\Pi_2\mathbf{q}''^2$, in addition to a single excitation, denoted by $\Pi_1 \mathbf{q}''$, where $\mathbf{q}'$ and $\mathbf{q}''$ are the coordinates of the IR and Raman active oscillators modes.

We consider the case in which the modes are both IR and Raman active, and hence $\mathbf{q} \propto \mathbf{q}' \sim \mathbf{q}''$. In the energy eigenstate representation, the vibrational mode is denoted by the bra state $\langle n|$ and the ket state $|m\rangle$ for the eigenenergies E_n and E_m, respectively. Then, the Liouville state is expressed as $|m\rangle\langle n|$. The coordinate state is expressed in terms of the creation and annihilation operators $\hat{a}^\dagger$ and $\hat{a}$ as $\mathbf{q} \propto (\hat{a}^\dagger + \hat{a})$. Then, the eigenstate $|n\rangle$ is converted into $|n+1\rangle$ and $|n-1\rangle$ by the linear IR and Raman excitations, while $|n\rangle$ is converted into $|n+2\rangle$ (two-quantum excitation), $|n-2\rangle$ (two-quantum de-excitation), and $|n\rangle$ (zero-quantum excitation) in the nonlinear case through $\mathbf{q}^2\,|n\rangle \propto [(\hat{a}^\dagger)^2 + \hat{a}^2 + \hat{a}^\dagger\hat{a} + \hat{a}\hat{a}^\dagger]\,|n\rangle$.[19–22]

Because the double excitation does not play a role in the THz excitation, there are fewer diagrams involved in 2D THz-Raman spectroscopy than in the 2D Raman case. We present representative diagrams of 2D TRT and 2D RTT response functions in Fig. 6. We note that the final state after the last interaction must be in a population state, $|n\rangle\langle n|$, because of the trace operation involved in the response function. The diagrams in Figs. 6(i) and 6(ii) arise from the first and second terms of Eq. (9), while the diagrams in Figs. 6(iii) and 6(iv) arise from the first and second terms of Eq. (10), respectively. The time propagator of each diagram without dissipation was also evaluated and displayed in each diagram of Fig. 6, where $E_1 - E_0 = \hbar\omega$ and $E_2 - E_1 = \hbar(\omega - \Delta)$.

For the lowest-order response cases depicted in Figs. 6(i) and 6(iii), the anharmonic interaction is represented by the green crosses. This interaction causes the excitation to different states without a laser interaction. The anharmonic interaction is essential for there to exist a signal at this order, because the Liouville paths do not terminate in the population state $|n\rangle\langle n|$ without it. The signal obtained from this contribution is elongated in the t_2 direction in the weak anharmonic case, due to the slow decay of the excitation through the anharmonic coupling over a period of length t_2.

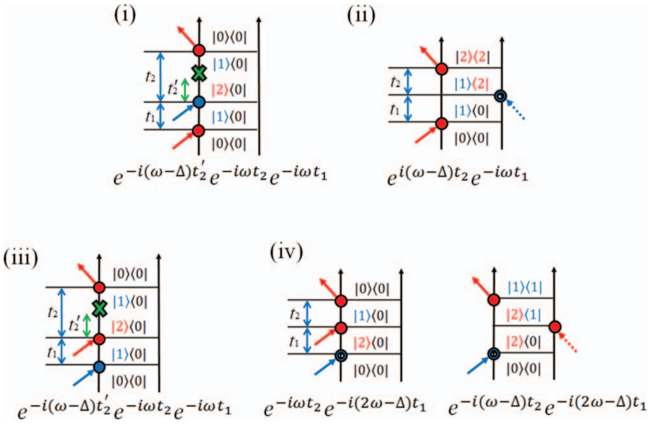

FIG. 6. Some representative optical Liouville paths involved in 2D THz-Raman-THz and Raman-THz-THz spectroscopy. Diagrams (i) and (ii) are from the first and second terms of Eq. (9), while diagrams (iii) and (iv) are from the first and second terms of Eq. (10), respectively. The red and blue arrows indicate THz and Raman excitations, respectively. Anharmonic interaction is indicted by the green crosses. The double circles represent the double quantum transition arising from the nonlinear polarizability of Raman excitation.

The diagrams in Figs. 6(i) and 6(ii) for the TRT signal exhibit different forms of time evolution, specifically, $\exp[-i\omega t_2]\exp[-i\omega t_1]$ and $\exp[i(\omega - \Delta)t_2]\exp[-i\omega t_1]$, respectively. The contribution displayed in Fig. 6(ii) exhibits an echo signal in a direction corresponding to $t_1 \approx t_2$ if the anharmonic contribution described by Fig. 6(i) is weak.

APPENDIX C: THE MOLECULAR POLARIZABILITY OF DMSO

In the DMSO case, the molecular polarizability $\boldsymbol{\alpha}$ for MD simulations was evaluated with *ab initio* calculations, which were carried out at B3LYP/6-311++G(3df, 3pd) level after optimizing the positions of the H atoms at the same level, while those of the other atoms were fixed with the same geometry as in the case of the rigid potential model presented in Ref. 90. We used the Gaussian 09 program package[92] to carry out *ab initio* calculations. Then, the polarizability was evaluated using sum-over-states perturbation theory (in units of Å^3) as[93–95]

$$\alpha = \begin{bmatrix} 9.6440 & 0.0000 & 0.0000 \\ 0.0000 & 8.5660 & 0.8928 \\ 0.0000 & 0.8928 & 7.3860 \end{bmatrix}, \tag{C1}$$

where the X axis is defined as that connecting the methyl groups (Me), the Y axis lies along the bisector of the Me-S-Me angle, and the Z axis is perpendicular to the XY plane. Here, the two methyl groups and the sulfur atom lie in the XY plane, and the oxygen atom is positioned in the positive Z direction. The average isotropic polarizability, $\overline{\alpha} = (\alpha_{xx} + \alpha_{yy} + \alpha_{zz})/3$, was found to be 8.5320 Å^3, which is slightly larger than the experimentally obtained value, 7.97 Å^3.[96,97]

APPENDIX D: TWO-DIMENSIONAL SIGNALS CALCULATED FROM A FOKKER-PLANCK EQUATION WITH A NONLINEAR SYSTEM-BATH INTERACTION

In this appendix, we demonstrate the difference between 2D TRT and 2D RTT signals based on a Brownian oscillator model with a nonlinear system-bath interaction that was introduced to take into account the effects of vibrational dephasing and relaxation,[23–27,63–66,98–101]

$$H_{tot} = \frac{\hbar\omega_0}{2}p^2 + U(q) + \sum_j \left[\frac{\hat{p}_j^2}{2m_j} + \frac{m_j\omega_j^2}{2} \times \left(\hat{x}_j - \frac{\alpha_j\left(V_{LL}q + \frac{1}{2}V_{SL}q^2\right)}{m_j\omega_j^2} \right)^2 \right], \tag{D1}$$

where p and q are the dimensionless coordinate and momentum,[14] $U(q)$ is the potential, and we introduced the fundamental frequency $\omega_0 \equiv U''(q)/\hbar$. The bath degrees of freedom are treated as an ensemble of harmonic oscillators, and the momentum, coordinate, mass, frequency, and the coupling strength between the system and the jth bath oscillator are given by $\hat{p}_j$, $\hat{x}_j$, m_j, ω_j, and α_j, respectively. The system-bath interaction is denoted by $H_I = -(V_{LL}q + \frac{1}{2}V_{SL}q^2)\sum_j \alpha_j \hat{x}_j$, where V_{LL} and V_{SL} are the linear-linear (LL) and square-linear (SL) system-bath coupling strength. As shown in Refs. 27 and 66, while the LL interaction mainly contributes to energy relaxation, the SL system-bath interaction leads to the vibrational dephasing for the slow modulation case due to the frequency fluctuation of system vibration. Here, we consider a classical Markovian heat-bath so that we can utilize a classical Markovian Fokker-Planck equation expressed as[23,27]

$$\begin{aligned}\frac{\partial}{\partial t}W(p,q;t) &= -p\frac{\partial}{\partial q}W(p,q;t) + \frac{1}{\hbar\omega_0}\frac{\partial U(q)}{\partial q}\frac{\partial}{\partial p}W(p,q;t)\\ &\quad + \frac{\zeta}{\omega_0}(V_{LL}+V_{SL}q)^2\frac{\partial}{\partial p}\left(p+\frac{k_BT}{\hbar\omega_0}\frac{\partial}{\partial p}\right)W(p,q;t), \qquad \text{(D2)}\end{aligned}$$

where T is the temperature and ζ is the system-bath coupling strength. We employ the same harmonic and Morse potentials with fundamental frequency, $\omega_0 = 38.7\ \mathrm{cm}^{-1}$, that were used in the previous studies of 2D Raman spectroscopy, except the curvature of the potential with $a = 0.0728$ for Morse potential.[14,27] We then chose the system-bath coupling parameters for $\zeta = 0.5\omega_0$ with $V_{LL} = 0$ and $V_{SL} = 1$ (pure dephasing case) and the temperature for $T = 300$ K. To calculate 2D THz-Raman signals, we expand the dipole moment $\mu(q) = \mu_1 q$ with $\mu_1 = 1$ and the polarizability $\Pi(q) = \Pi_1 q + \Pi_2 q^2$ with $\Pi_1 = -1$ and $\Pi_2 = 0.05$, respectively. Using the procedure explained in Refs. 23–26, and 27, we calculate the 2D TRT and RTT signals defined in Eqs. (1) and (2), respectively. These results are presented in Fig. 7.

The signal in the TRT and RTT regions in the harmonic case arises from $\mu_1^2\Pi_2\langle[q(t_1+t_2),[q^2(t_1),q(0)]]\rangle$ and $\mu_1^2\Pi_2\langle[q(t_1+t_2),[q(t_1),q^2(0)]]\rangle$, whereas those in the Morse case have the contributions from the anharmonicity expressed as the second terms in Eqs. (9) and (10), respectively. The difference between the Morse and harmonic case clearly indicates that the elongation of the peak in the t_2 direction in the Morse case occurs due to the anharmonicity of the vibrational mode. In the TRT region in Fig. 7(a), the anharmonic contribution appears for large time t_2, while the nonlinear polarizability, $\mu_1^2\Pi_2\langle[q(t_1+t_2),[q^2(t_1),q(0)]]\rangle$ is dominant for small time t_2. In the RTT region, however, the contribution from the nonlinear polarizability is so small that the signal is dominated by the anharmonic contribution. This indicates that the contribution from $\mu_1^2\Pi_2\langle[q(t_1+t_2),[q^2(t_1),q(0)]]\rangle$ plays more important role than $\mu_1^2\Pi_2\langle[q(t_1+t_2),[q(t_1),q^2(0)]]\rangle$ in the 2D THz-Raman spectroscopy.

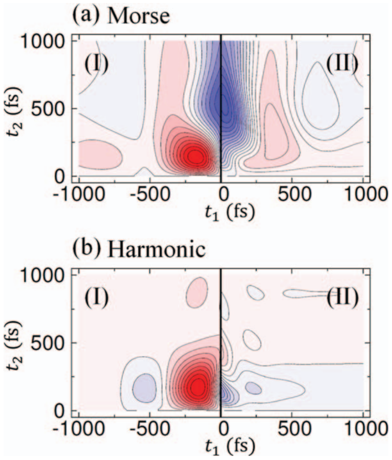

FIG. 7. The profiles of (I) 2D THz-Raman-THz (TRT) and (II) 2D Raman-THz-THz (RTT) for (a) Morse and (b) harmonic oscillator with a nonlinear system-bath interaction, respectively. Positive and negative signals are represented by red and blue colors, respectively, and the time axis t_1 has been inverted in the TRT cases. The TRT and RTT signals have been normalized with respect to the maximum peak intensity of the TRT signal.

For the calculations presented here, we assumed a Markovian noise bath. Therefore, the memory time of the fluctuations is zero and there is no echo feature predicted, neither in the TRT nor in the RTT signals. Although computationally more expensive, it is possible to use hierarchy of equations of motion to take into account the non-Markovian and non-perturbative fluctuation to calculate the TRT and RTT signals separately.[24–27]

[1] S. T. Cundiff and S. Mukamel, Phys. Today **66**, 44 (2013).
[2] S. Mukamel, Y. Tanimura, and P. Hamm, Acc. Chem. Res. **42**, 1207 (2009).
[3] S. Mukamel, *Principles of Nonlinear Optical Spectroscopy* (Oxford University Press, Oxford, 1995).
[4] Y. Tanimura and S. Mukamel, J. Chem. Phys. **99**, 9496 (1993).
[5] S. Palese, J. T. Buontempo, L. Schilling, W. T. Lotshaw, Y. Tanimura, S. Mukamel, and R. J. D. Miller, J. Chem. Phys. **98**, 12466 (1994).
[6] K. Okumura and Y. Tanimura, J. Chem. Phys. **106**, 1687 (1997).
[7] K. Okumura and Y. Tanimura, J. Chem. Phys. **107**, 2267 (1997).
[8] K. Okumura and Y. Tanimura, Chem. Phys. Lett. **277**, 159 (1997).
[9] M. Cho, K. Okumura, and Y. Tanimura, J. Chem. Phys. **108**, 1326 (1998).
[10] A. Piryatinski, V. Chernyak, and S. Mukamel, Chem. Phys. **266**, 311 (2001).
[11] V. Khidekel, V. Chernyak, and S. Mukamel, J. Chem. Phys. **105**, 8543 (1996).
[12] S. Hahn, K. Park, and M. Cho, J. Chem. Phys. **111**, 4121 (1999).
[13] K. Park, M. Cho, S. Hahn, and D. Kim, J. Chem. Phys. **111**, 4131 (1999); M. Cho, *ibid.* **111**, 4140 (1999).
[14] Y. Tanimura, Chem. Phys. **233**, 217 (1998).
[15] K. Okumura and Y. Tanimura, Chem. Phys. Lett. **278**, 175 (1997).
[16] A. Tokmakoff, M. J. Lang, D. S. Larsen, G. R. Fleming, V. Chernyak, and S. Mukamel, Phys. Rev. Lett. **79**, 2702 (1997).
[17] S. Hahn, K. Park, and M. Cho, J. Chem. Phys. **111**, 4121 (1999).
[18] K. Okumura, A. Tokmakoff, and Y. Tanimura, J. Chem. Phys. **111**, 492 (1999).
[19] T. Steffen, J. T. Fourkas, and K. Duppen, J. Chem. Phys. **105**, 7364 (1996).
[20] T. Steffen and K. Duppen, Chem. Phys. **233**, 267 (1998).
[21] J. T. Fourkas, Adv. Chem. Phys. **117**, 235 (2001).
[22] K. Okumura and Y. Tanimura, J. Phys. Chem. A **107**, 8092 (2003).
[23] T. Steffen and Y. Tanimura, J. Phys. Soc. Jpn. **69**, 3115 (2000).
[24] Y. Tanimura and T. Steffen, J. Phys. Soc. Jpn. **69**, 4095 (2000).
[25] T. Kato and Y. Tanimura, J. Chem. Phys. **117**, 6221 (2002).
[26] T. Kato and Y. Tanimura, J. Chem. Phys. **120**, 260 (2004).
[27] Y. Tanimura, J. Phys. Soc. Jpn. **75**, 082001 (2006).
[28] S. Saito and I. Ohmine, J. Chem. Phys. **108**, 240 (1998).
[29] I. Ohmine and S. Saito, Acc. Chem. Res. **32**, 741 (1999); Erratum **32**, 825 (1999).
[30] A. Ma and R. M. Stratt, Phys. Rev. Lett. **85**, 1004 (2000).
[31] A. Ma and R. M. Stratt, J. Chem. Phys. **116**, 4962 (2002).
[32] A. Ma and R. M. Stratt, J. Chem. Phys. **116**, 4972 (2002).
[33] S. Saito and I. Ohmine, Phys. Rev. Lett. **88**, 207401 (2002).
[34] S. Saito and I. Ohmine, J. Chem. Phys. **119**, 9073 (2003).
[35] S. Saito and I. Ohmine, J. Chem. Phys. **125**, 084506 (2006).

[36] Y. Nagata and Y. Tanimura, J. Chem. Phys. **124**, 024508 (2006).
[37] Y. Nagata, T. Hasegawa, and Y. Tanimura, J. Chem. Phys. **124**, 194504 (2006).
[38] Y. Nagata, Y. Tanimura, and S. Mukamel, J. Chem. Phys. **126**, 204703 (2007).
[39] T. I. C. Jansen, J. G. Snijders, and K. Duppen, J. Chem. Phys. **114**, 10910 (2001).
[40] T. I. C. Jansen, K. Duppen, and J. G. Snijders, Phys. Rev. B **67**, 134206 (2003).
[41] T. Hasegawa and Y. Tanimura, J. Chem. Phys. **125**, 074512 (2006).
[42] M. Kryvohuz and J. Cao, J. Chem. Phys. **122**, 024109 (2005).
[43] M. Kryvohuz and J. Cao, Phys. Rev. Lett. **95**, 180405 (2005).
[44] D. A. Blank, L. J. Kaufman, and G. R. Fleming, J. Chem. Phys. **111**, 3105 (1999).
[45] D. A. Blank, L. J. Kaufman, and G. R. Fleming, J. Chem. Phys. **113**, 771 (2000).
[46] O. Golonzka, N. Demirdoven, M. Khalili, and A. Tokmakoff, J. Chem. Phys. **113**, 9893 (2000).
[47] L. J. Kaufman, J. Heo, L. D. Ziegler, and G. R. Fleming, Phys. Rev. Lett. **88**, 207402 (2002).
[48] K. J. Kubarych, C. J. Milne, and R. J. D. Miller, Int. Rev. Phys. Chem. **22**, 497 (2003).
[49] K. J. Kubarych, C. L. Milne, S. Lin, V. Astinov, and R. J. D. Miller, J. Chem. Phys. **116**, 2016 (2002).
[50] K. J. Kubarych, C. L. Milne, and R. J. D. Miller, Chem. Phys. Lett. **369**, 635 (2003).
[51] C. L. Milne, Y. L. Li, T. L. C. Jansen, L. Huang, and J. D. Miller, J. Phys. Chem. B **110**, 19867 (2006).
[52] Y. L. Li, L. Huang, R. J. D. Miller, T. Hasegawa, and Y. Tanimura, J. Chem. Phys. **128**, 234507 (2008).
[53] P. Hamm, M. Lim, and R. M. Hochstrasser, J. Phys. Chem. B **102**, 6123 (1998).
[54] S. Woutersen and P. Hamm, J. Phys. Chem. B **104**, 11316 (2000).
[55] M. T. Zanni, S. Gnanakaran, J. Stenger, and R. M. Hochstrasser, J. Phys. Chem. B **105**, 6520 (2001).
[56] M. Khalil, N. Demirdoven, and A. Tokmakoff, J. Phys. Chem. A **107**, 5258 (2003).
[57] K. Ohta, H. Maekawa, S. Saito, and K. Tominaga, J. Phys. Chem. A **107**, 5643 (2003).
[58] K. A. Merchant, W. G. Noid, D. E. Thompson, R. Akiyama, R. F. Loring, and M. D. Fayer, J. Phys. Chem. B **107**, 4 (2003).
[59] J. B. Asbury, T. Steinel, C. Stromberg, S. A. Corcelli, C. P. Lawrence, J. L. Skinner, and M. D. Fayer, J. Phys. Chem. A **108**, 1107 (2004).
[60] B. Auer, R. Kumar, J. R. Schmidt, and J. L. Skinner, Proc. Natl. Acad. Sci. U.S.A. **104**, 14215 (2007).
[61] S. Garrett-Roe, F. Perakis, F. Rao, and P. Hamm, J. Phys. Chem. B **115**, 6976 (2011).
[62] F. Perakis and P. Hamm, J. Phys. Chem. B **115**, 5289 (2011).
[63] A. Ishizaki and Y. Tanimura, J. Chem. Phys. **125**, 084501 (2006).
[64] A. Ishizaki and Y. Tanimura, J. Phys. Chem. A **111**, 9269 (2007).
[65] A. Sakurai and Y. Tanimura, J. Phys. Chem. A **115**, 4009 (2011).
[66] Y. Tanimura and A. Ishizaki, Acc. Chem. Res. **42**, 1270 (2009).
[67] T. Yagasaki and S. Saito, Acc. Chem. Res. **42**, 1250 (2009).
[68] T. Yagasaki and S. Saito, J. Chem. Phys. **134**, 184503 (2011).
[69] T. Yagasaki and S. Saito, Annu. Rev. Phys. Chem. **64**, 55 (2013).
[70] N. Huse, S. Ashihara, E. T. J. Nibbering, and T. Elsaesser, Chem. Phys. Lett. **404**, 389 (2005).
[71] S. Ashihara, N. Huse, A. Espagne, E. T. J. Nibbering, and T. Elsaesser, Chem. Phys. Lett. **424**, 66 (2006).
[72] S. Ashihara, N. Huse, A. Espagne, E. T. J. Nibbering, and T. Elsaesser, J. Phys. Chem. A **111**, 743 (2007).
[73] K. Okumura and Y. Tanimura, Chem. Phys. Lett. **295**, 298 (1998).
[74] Y. Suzuki and Y. Tanimura, J. Chem. Phys. **128**, 164501 (2008).
[75] W. Kuehn, K. Reimann, M. Woerner, and T. Elsaesser, J. Chem. Phys. **130**, 164503 (2009).
[76] W. Kuehn, K. Reimann, M. Woerner, T. Elsaesser, and R. Hey, J. Phys. Chem. B **115**, 5448 (2011).
[77] W. Kuehn, K. Reimann, M. Woerner, T. Elsaesser, R. Hey, and U. Schade, Phys. Rev. Lett. **107**, 067401 (2011).
[78] P. Hamm and J. Savolainen, J. Chem. Phys. **136**, 094516 (2012).
[79] P. Hamm, J. Savolainen, J. Ono, and Y. Tanimura, J. Chem. Phys. **136**, 236101 (2012).
[80] J. Savolainen, S. Ahmed, and P. Hamm, Proc. Natl. Acad. Sci. U.S.A. **110**, 20402 (2013).
[81] T. Hasegawa and Y. Tanimura, J. Chem. Phys. **128**, 064511 (2008).
[82] B. M. Ladanyi, Chem. Phys. Lett. **121**, 351 (1985).
[83] J. Applequist, J. R. Carl, and K.-K. Fung, J. Am. Chem. Soc. **94**, 2952 (1972).
[84] J. L. F. Abascal and C. Vega, J. Chem. Phys. **123**, 234505 (2005).
[85] R. Walser, A. E. Mark, W. F. van Gunsteren, M. Lauterbach, and G. Wipff, J. Chem. Phys. **112**, 10450 (2000).
[86] K. P. Sagarik and R. Ahlrichs, J. Chem. Phys. **86**, 5117 (1987).
[87] M. C. Wojcik, K. Hermansson, and H. O. G. Siegbahn, J. Chem. Phys. **113**, 3374 (2000).
[88] J. Richardi, P. H. Fries, and H. Krienke, J. Chem. Phys. **108**, 4079 (1998).
[89] B. Collignon and S. Picaud, Chem. Phys. Lett. **393**, 457 (2004).
[90] H. Liu, F. Muller-Plathe, and W. F. van Gunsteren, J. Am. Chem. Soc. **117**, 4363 (1995).
[91] C. Huiszoon, Mol. Phys. **58**, 865 (1986).
[92] M. J. Frisch, G. W. Trucks, H. B. Schlegel *et al.*, Gaussian 09, Revision D.01, Gaussian, Inc., Wallingford, CT, 2009.
[93] T. Helgaker, P. Jorgensen, and J. Olsen, *Molecular Electronic-Structure Theory* (Wiley, New York, 2000).
[94] J. Autschbach and T. Ziegler, Coord. Chem. Rev. **238**, 83 (2003).
[95] F. Jensen, *Introduction to Computational Chemistry* (Wiley, New York, 2006).
[96] P. J. Pacak, J. Solution Chem. **16**, 71 (1987).
[97] K. J. Miller, J. Am. Chem. Soc. **112**, 8533 (1990).
[98] D. W. Oxtoby, Adv. Chem. Phys. **40**, 1 (1979).
[99] D. W. Oxtoby, Adv. Chem. Phys. **47**, 487 (1981).
[100] J. S. Bader and B. J. Berne, J. Chem. Phys. **100**, 8359 (1994).
[101] K. Okumura and Y. Tanimura, Phys. Rev. E **56**, 2747 (1997).